




Article

Carbonate and cation substitutions in hydroxylapatite in breast cancer micro-calcifications

Yan Zhang^{1,†} , Changqiu Wang^{1,†}, Yan Li^{1,*}, Anhuai Lu^{1,*}, Fanlu Meng¹, Hongrui Ding¹, Fang Mei², Jianying Liu², Kang Li³, Chongqing Yang⁴, Jingyun Du⁵ and Yanzhang Li¹

¹Key Laboratory of Orogenic Belts and Crustal Evolution, Beijing Key Laboratory of Mineral Environmental Function, School of Earth and Space Sciences, Peking University, Beijing 100871, China; ²Pathology Department, School of Basic Medical Science, Health Science Center of Peking University, Beijing 100083, China; ³Department of Cardiology, Beijing Hospital, Beijing 100730, China; ⁴Department of Pathology, Beijing Hospital, Beijing 100730, China; and ⁵Department of Pathology, Yidu Hospital of Traditional Chinese Medicine, Hubei, 443300, China

Abstract

Calcification within breast cancer is a diagnostically significant radiological feature that generally consists of hydroxylapatite. Samples from 30 cases of breast carcinoma with calcification were investigated using optical microscopy, energy-dispersive X-ray analysis, transmission-electron microscopy, Fourier-transform infrared spectroscopy, Raman spectroscopy, synchrotron radiation X-ray diffraction and X-ray fluorescence. Under optical microscopy, the calcifications were found to consist of either irregular aggregates with widths > 200 μm or spherical aggregates similar to psammoma bodies with an average diameter of 30 μm . Transmission-electron microscopy showed that short columnar or dumbbell-shaped crystals with widths of 10–15 nm and lengths of 20–50 nm were the most common morphology; spherical aggregates ($\sim 1 \mu\text{m}$ in diameter) with amorphous coatings of fibrous nanocrystals were also observed. Results indicated that hydroxylapatite was the dominant mineral phase in the calcifications, and both CO_3^{2-} and cation substitutions (Na, Mg, Zn, Fe, Sr, Cu and Mn) were present in the hydroxylapatite structure. Fourier-transform infrared spectra show peaks at 872 and 880 cm^{-1} indicating that CO_3^{2-} substituted both the OH^- (A type) and PO_4^{3-} (B type) sites of hydroxylapatite, making it an A and B mixed type. The ratio of B- to A-type substitution was estimated in the range of 1.1–18.7 from the ratio of peak intensities (I_{872}/I_{880}), accompanied with CO_3^{2-} contents from 1.1% to 14.5%. Trace arsenic, detected *in situ* by synchrotron radiation X-ray fluorescence was found to be distributed uniformly in the calcifications in the form of AsO_4^{3-} substituting for PO_4^{3-} . It is therefore proposed that identifying these trace elements in breast cancer calcifications may be promising for future clinical diagnostics.

Keywords: breast carcinoma, hydroxylapatite, carbonate, bioapatite, isomorphous substitution, trace element, B-type substitution

(Received 26 December 2020; accepted 8 March 2021; Accepted Manuscript published online: 11 March 2021; Associate Editor: Runliang Zhu)

Introduction

Breast cancer is one of the most common cancers worldwide. Statistics from 185 countries in 2018 reported there were ~ 2.1 million newly diagnosed female breast cancer cases, accounting for almost 1 in 4 cancer cases among women. The disease is also the leading cause of cancer death in over 100 countries (Bray *et al.*, 2018). It is generally diagnosed and evaluated with mammography, in which calcification is a significant diagnostic feature (Obenaus *et al.*, 2005). Clinically, calcifications are classified according to the categories described in the Breast Imaging Reporting and Data System lexicon by the American College of Radiology (Gülsün *et al.*, 2003). Benign calcifications (generally recognised by their size, shape and distribution) are usually pathognomonic signs that allow malignancy to be excluded with high

probability (Lieberman *et al.*, 1998; Kaltenbach *et al.*, 2017). In the absence of recognisably benign calcifications, follow-up biopsies and pathological examination are required to examine the cellular morphology and detect smaller micro-calcifications (Obenaus *et al.*, 2005; Kaltenbach *et al.*, 2017).

The introduction of the methods of mineralogy or materials science to the study of breast cancer calcifications has contributed substantially to their identification (Kaltenbach *et al.*, 2017; Kunitake *et al.*, 2018). Researchers in histopathology have found that breast cancer calcifications mainly consist of hydroxylapatite with the general formula $\text{Ca}_5(\text{PO}_4)_3(\text{OH})$ (Morgan *et al.*, 2001; Gosling *et al.*, 2019), except for some exceptional examples where calcium oxalate or weddellite ($\text{Ca}(\text{C}_2\text{O}_4) \cdot (2.5-x)\text{H}_2\text{O}$; Mills and Christy, 2016) have been found in carcinoma *in situ* (Frappart *et al.*, 1987; Haka *et al.*, 2002), a type of non-invasive or precancerous growth. Recent studies have described and linked the carbonate content of breast cancer calcifications in pathological breast disease to the invasive cancer grades (grades 1, 2 and 3) and stages of ductal carcinoma *in situ* (low, intermediate and high grade) (Baker *et al.*, 2010; Sathyavathi *et al.*, 2015), heightening interest in the detailed mineralogical characteristics of calcifications in breast cancer.

†The first two authors contributed equally to this paper.

*Authors for correspondence: Yan Li, Email: liyan-pku@pku.edu.cn; Anhuai Lu, Email: ahlu@pku.edu.cn

Cite this article: Zhang Y., Wang C., Li Y., Lu A., Meng F., Ding H., Mei F., Liu J., Li K., Yang C., Du J. and Li Y. (2021) Carbonate and cation substitutions in hydroxylapatite in breast cancer micro-calcifications. *Mineralogical Magazine* 85, 321–331. <https://doi.org/10.1180/mgm.2021.23>

Hydroxylapatite is a typical product of biomineralisation (Weiner and Dove, 2003; Achal *et al.*, 2015). It belongs to the apatite supergroup with a hexagonal structure, and its chemical formula is usually written as $\text{Ca}_{10}(\text{PO}_4)_6(\text{OH})_2$ (Pasero *et al.*, 2010). In practice, however, the Ca:P ratio is seldom equal to the ideal 1.67, and Ca:P ratios in the range from 1.33 to 1.95 have been reported after accounting for instrument and resolution error (McConnell, 1960; Baikie *et al.*, 2009). This wide variation is caused by structural defects, such as calcium vacancies (Ivanova *et al.*, 2001) or isomorphous substitutions at Ca sites (Get'man *et al.*, 2010), tetrahedral sites (Pan and Fleet, 2002), or in the hexagonal channel (Ito *et al.*, 1997) of hydroxylapatite. Accordingly, some differences in the crystal-lattice parameters, micromorphology, microstructure and biological effects have been documented in hydroxylapatite with different defects or defect densities (Legeros *et al.*, 1967; Barralet *et al.*, 1998; Webster *et al.*, 2002; Obadia *et al.*, 2003; Li *et al.*, 2007). Notably, the effects of anion substitution on the structure and physicochemical properties of hydroxylapatite are also significant, particularly the substitution of carbonate ions (CO_3^{2-}). Two substitution sites for CO_3^{2-} in apatite classify the apatite into A, B, and A–B type substitutions with OH^- , PO_4^{3-} and both substituted (LeGeros *et al.*, 1969; Vignoles *et al.*, 1988; Fleet and Liu, 2003), respectively (see Fig. 1). Further details on ion substitution in hydroxylapatite in breast cancer calcifications are needed to elucidate the links between the occurrence and development of the calcifications, to improve the diagnosis of breast cancer, and even to enable the treatment of breast cancer using targeted medicine or approaches to decomposing hydroxylapatite-related calcifications or inhibiting their growth (Morgan *et al.*, 2001; Cook *et al.*, 2003; Peroos *et al.*, 2006; Awonusi *et al.*, 2007; Fleet, 2009; Fleet *et al.*, 2011; Madupalli *et al.*, 2017).

Various techniques have been used to study the mineralogical characteristics of hydroxylapatite and its substitutions. Hydroxylapatite with Ca:P ratios as low as 1.51 and as high as 1.71 may produce almost indistinguishable patterns in powder X-ray diffraction (XRD) (Raynaud *et al.*, 2002). Although the structure of hydroxylapatite with isomorphous substitutions showed certain distinctions after refinement by the Rietveld method (LeGeros *et al.*, 1976; El Feki *et al.*, 1999; El Feki *et al.*, 2000; White and Dong, 2003; Get'man *et al.*, 2010; Lala *et al.*, 2016; Cheng *et al.*, 2019; Baldassarre *et al.*, 2020), identification of the exact substituting ions (groups) in apatite samples remain difficult using XRD analyses alone. Fourier-transform infrared spectroscopy (FTIR), Raman spectroscopy, and thermogravimetric analyses (TGA) coupled with differential thermal analysis (DTA) are often employed to study CO_3^{2-} in hydroxylapatite (Raynaud *et al.*, 2002). Cations can be detected directly by energy-dispersive X-ray analysis (EDAX), electron-probe microanalysis (EPMA), laser-ablation inductively coupled plasma mass spectrometry (LA-ICP-MS) and X-ray fluorescence (XRF) (Belousova *et al.*, 2002; Shen *et al.*, 2012). However, bulk methods such as traditional XRD, TGA-DTA, ICP-MS, FTIR pellet methods, and traditional XRF are not appropriate for doing analyses of breast cancer calcifications due to their micro- or nano-particle size and extremely limited quantities. Furthermore, the spot sizes used in EPMA and LA-ICP-MS are not small enough. Analyses of calcifications using conventional X-ray absorption spectroscopy are also difficult due to small sample sizes and their uneven compositions. As a result of these limitations on sample size, quantity, and uniformity, mineralogical studies on breast cancer calcifications have not yet been extensively and thoroughly conducted. In this study, we established a comprehensive range of micro-regional research methods

to characterise these calcifications, focusing mainly on isomorphous substitutions to hydroxylapatite in the calcifications, and comparing the characteristics of breast cancer calcifications with samples of synthetic and natural hydroxylapatite.

Materials and methods

An optical microscope was used to select 30 cases of breast carcinoma with calcification by observing thin sections stained with hematoxylin and eosin (H&E). The paraffin-embedded samples were obtained from the Department of Pathology, Peking University Health Science Center (PUHSC). The samples were collected with the permission of the patients, and the study as a whole was approved by PUHSC. Pathological diagnosis was performed using at least two experienced pathologists at PUHSC.

Preparation of section samples

Thin sections of 4 or 10 μm in thickness and $\sim 15\text{ mm} \times 15\text{ mm}$ in area were obtained using a Leica ultramicrotome. Ordinary 4 μm H&E sections were prepared for observation under optical microscopy, and 10 μm sections were loaded on clean 20 mm \times 20 mm silicon wafers for environmental scanning-electron microscopy and EDAX (with exposure times of 10 or 30 s). The samples were soaked in xylene to remove the paraffin, and absolute ethanol was used to remove the xylene. Details of the procedures can be found in Wang *et al.* (2011).

Separation of powder samples

To avoid interference by organics, dozens of slices were processed to separate the calcifications from the surrounding tissues. Minerals were separated from organic tissues following the method described in Wang *et al.* (2011). Briefly, slices of the serial sections were put into a 1.5 mL centrifuge tube and soaked with xylene for 24 h, 12 h and then 5 h. Ethanol in graded concentrations of 100%, 95%, 90%, 85%, 70%, 50% and 30% was separately and sequentially added to remove the xylene for 10 min in each grade. Subsequently, the samples were washed with distilled water three times and twice digested in 5% sodium hypochlorite solution in a 37°C water bath for 30 min. Finally, the remaining powders were washed with distilled water four times and dehydrated in graded ethanol of 50%, 65%, 75%, 85%, 95%, 100%, and 100% for 15 min, 25 min, 35 min, 15 min, 25 min, 30 min and 40 min, respectively. The powder samples were stored in ethanol under room temperature.

Methods for mineralogical characterisation

Transmission electron microscopy (TEM) was performed using a TECNAIF 30 with an operating voltage of 300 kV and a JEM-2100F with an operating voltage of 200 kV. The samples were prepared for analyses by dripping $\sim 0.1\text{ mL}$ suspension with powder samples and absolute ethanol onto carbon-coated copper grids. The data were processed and analysed with *Digital Micrograph* version 3.6.5 (Gatan Ltd.). Micro Fourier-transform infrared spectroscopy (FTIR) was conducted using a NICOLET iN10 MX Micro-FTIR spectrometer. The spectra were collected in transmission mode with a resolution of 4 cm^{-1} over the 600–4000 cm^{-1} spectral range.

The Raman measurements were carried out using a Renishaw InVia system attached to a Leica microscope (50 \times objective) with a two-dimensional CCD camera. A 532 nm laser-excitation wavelength

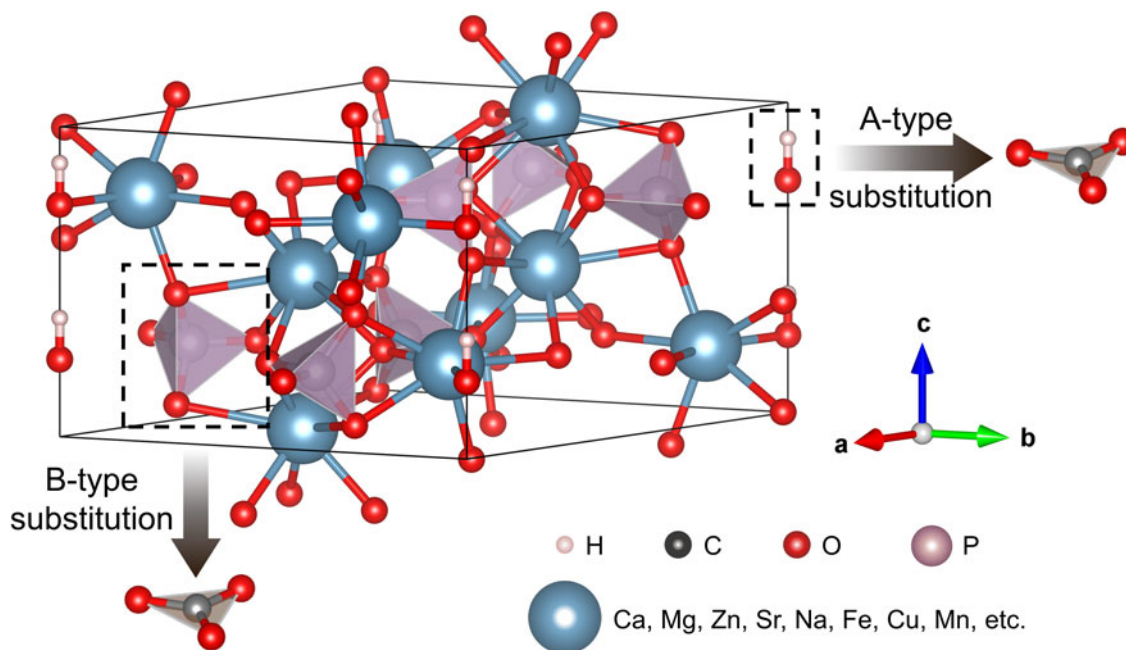


Fig. 1. The crystal structure diagram of hydroxylapatite with cation substitution and carbonate group substitution as A or B type.

and high-resolution gratings (2400 gr/mm) were employed. Raman scattering maps were collected using the Renishaw StreamLine accessory with a step size of 1.3 μm . The exposure time for each spot was 10 s. The data processing was conducted with WiRE 4.1 (Renishaw).

Synchrotron radiation XRD (SR-XRD) and XRF (SR-XRF) were performed at the BL15U beamline of the Shanghai Synchrotron Radiation Facility (SSRF) in Shanghai, China. Powder samples were mounted between two pieces of 3M film after ethanol volatilisation and then attached to the sample holder. Angle-dispersive SR-XRD experiments were performed using a wavelength of 0.6884 \AA , a focused beam size of $\sim 5 \mu\text{m} \times 10 \mu\text{m}$, and a Mar CCD detector. CeO_2 was used to calibrate the wavelength of the X-rays and to determine the distance from the sample to the detector, as well as other parameters. The collection time for each SR-XRD pattern was 20–100 s. All collected images were integrated with *Fit2D V12.077* (Hammersley A.P., 1997) to obtain conventional one-dimensional diffraction spectra. XRD data processing and phase identification were achieved by *Highscore Plus* software (version 4.6.1) (Malvern Panalytical, the Netherlands). SR-XRF was conducted under fluorescence mode with a 50 mm^2 silicon-drift detector (Vortex, USA) with air in the ion chamber. The energy for the SR-XRF test was 18 keV, and the focused beam size was 4 $\mu\text{m} \times 4.5 \mu\text{m}$. The collection time for each SR-XRF pattern was 100 s, and all collected data were analysed with the software *PyMca* (Version 4.4.0, Solé *et al.*, 2007). Samples for SR-XRF mapping were transferred from the aforementioned silicon wafers to Kapton films, and the collection time for each point in the element mapping was 8 s. The detection limit of SR-XRF in the BL15U beamline can reach the level of $\mu\text{g/g}$ with an energy resolution of 0.2 eV.

Results

Mineral phase and crystal structure

Breast cancer calcifications appeared dark purple in H&E-stained sections under optical microscopy (Fig. 2). Their profiles were either irregular (Fig. 2a) or spherical (Fig. 2b, c). The irregular

calcifications were always greater than 200 μm across and they were usually associated with necrosis; the spherical calcifications were similar to psammoma bodies and had an average size of 30 μm . Both irregular and spherical calcifications appeared to be generally present in breast cancer for stages T1, T2 and T3. The stages were judged according to the size of the tumour, following World Health Organization (2017) protocols.

The mineral phases of the calcifications were identified using SR-XRD. As shown in Fig. 3, the diffraction pattern for the calcifications were indexed as hydroxylapatite ($\text{Ca}_5(\text{PO}_4)_3(\text{OH})$), using PDF#09-0432 (powder diffraction file from the International Centre for Diffraction Data, <http://www.icdd.com/>). Compared to the standards for hydroxylapatite and carbonated hydroxylapatite ('CHA', $\text{Ca}_5[\text{PO}_4\text{CO}_3]_3(\text{OH})$, PDF#19-0272), slight shifts and widening of the peaks corresponding to the (002), (211) and (202) faces were evident, suggesting poor crystallinity, or interference from organic residues. These factors made it difficult to determine whether the sample best matched hydroxylapatite or CHA.

The fine structure of separated calcifications was examined using TEM. In all cases, the dominant morphology of the aggregates was short columnar or dumbbell-shaped crystals with widths of 10–15 nm and lengths of 20–50 nm (Fig. 4a, dotted line). Both lattice fringe images (Fig. 4b) and diffraction patterns (Fig. 4c) showed the two dominant interplanar distances as 3.36 and 2.89 \AA , which are matched well to the (002) and (211) planes of hydroxylapatite (PDF#09-0432), respectively. Notably, compared with lattice parameters of hydroxylapatite, standard CHA (PDF#19-0272) has slightly larger c and smaller a , resulting in its larger (002) spacing (3.46 \AA) and smaller (211) spacing (2.79 \AA). Therefore, the main phase of most aggregates observed in TEM should be hydroxylapatite; some minor CHA might co-exist and cannot be ruled out. The multiple domains in the lattice photograph and the rings in the diffraction pattern show that these short columnar or dumbbell-like crystals are polycrystalline aggregates.

Spherical aggregates (Fig. 4d) in a sample from an 86-year-old woman were larger than 1 μm in diameter, similar to the

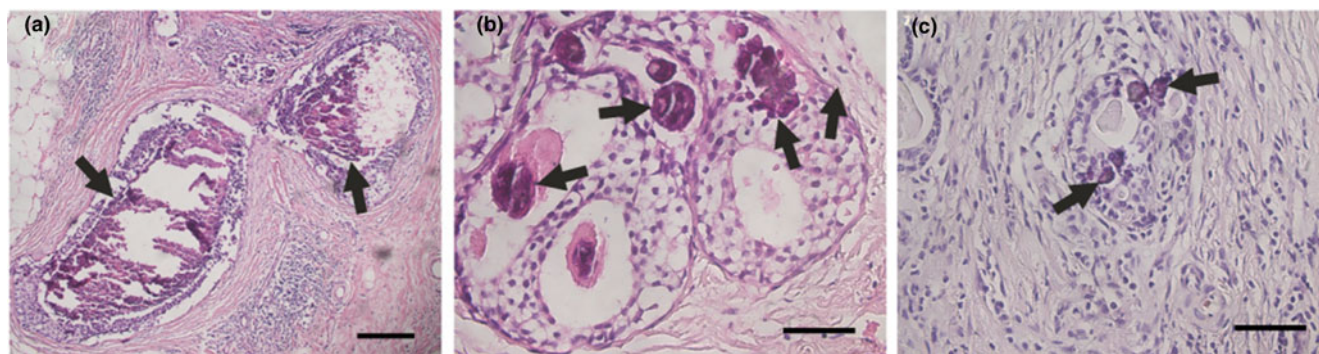


Fig. 2. Calcifications (indicated by arrows) in optical microscopy images of breast carcinoma. (a) Irregular calcifications in a stage T1 breast carcinoma. (b) Spherical calcifications in a stage T2 breast carcinoma. (c) Spherical calcifications in a stage T3 breast carcinoma. Scale bars: (a) 200 μm ; (b, c) 50 μm .

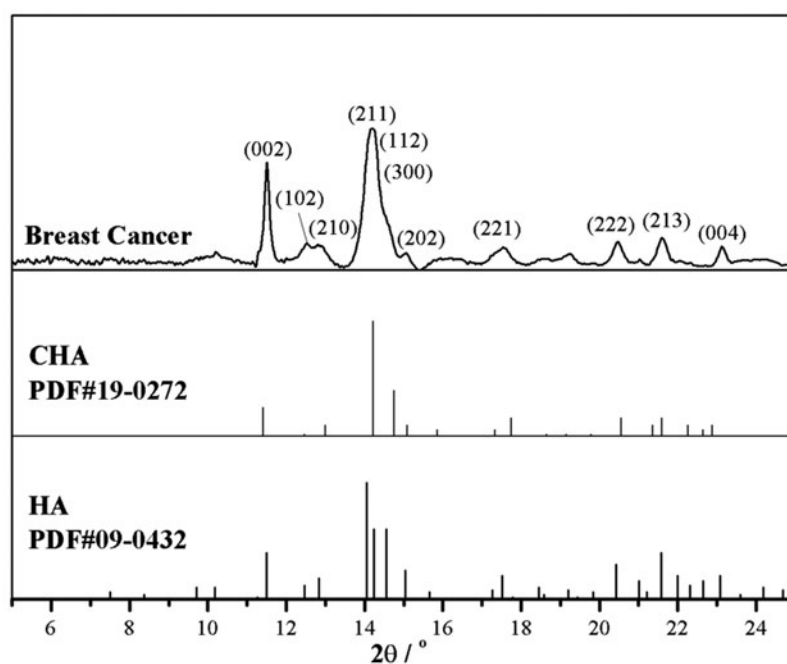


Fig. 3. SR-XRD pattern of a breast cancer calcification and comparison with standards: CHA - carbonated hydroxylapatite (PDF#19-0272) and HA - hydroxylapatite, $\text{Ca}_5(\text{PO}_4)_3(\text{OH})$, (PDF#09-0432).

psammoma bodies. The outer part of the particles was amorphous and was thinner than the centre. An enlarged view showed that the surface of the spherical aggregates consisted of fibrous nanocrystals whose longitudinal axis was oriented towards the centre of the sphere (Fig. 4e). Two dominating diffraction patterns for fibrous nanocrystals, belonging to (002) and (211) planes, also confirmed the presence of hydroxylapatite as the main crystallised phase (Fig. 4f). Notably, the degree of crystallinity for the fibrous nanocrystal aggregates was poor relative to the crystallinity of the columnar and dumbbell-shaped crystals.

Carbonate substitution

According to the EDAX results (Table 1) for section samples on silicon wafers, the major elements present in the calcifications were carbon (C), oxygen (O), calcium (Ca) and phosphorus (P). The Ca:P ratio (atomic percentage) varied from 1.13 to 2.35. Raman spectra, Raman mappings, and FTIR spectra of the calcifications, are shown in Figs 5–7, respectively. According to previous research (Penel *et al.*, 1998; Awonusi *et al.*, 2007; Antonakos *et al.*,

2007; Wang *et al.*, 2018), the single Raman band for $\nu_1(\text{PO}_4^{3-})$ near 960 cm^{-1} , the two bands near 432 and 445 cm^{-1} for $\nu_2(\text{PO}_4^{3-})$, and the $\nu_1(\text{CO}_3^{2-})$ band near 1071 cm^{-1} are specific to B-type CO_3^{2-} substitution (PO_4^{3-} substituted by CO_3^{2-}) (Fig. 5a). A comparison of the 432 and 445 cm^{-1} bands for the breast cancer calcifications (Fig. 5b) with those of reference spectra (Fig. 5d) showed that the CO_3^{2-} substitution was mainly of the B type, and a comparison of the band near 1071 cm^{-1} in the experimental (Fig. 5c) and reference (Fig. 5e) spectra confirmed that B-type CO_3^{2-} substitution was present in the hydroxylapatite of the calcification.

The distributions of CO_3^{2-} and PO_4^{3-} were obtained from Raman scattering mappings of tissue sections. Calcifications appeared as bright white regions in optical microscopy images (Fig. 6a), and organic tissues appeared dark in the images. According to the spectral characteristics of the Raman imaging test, the substitution amount of PO_4^{3-} was examined at its peak intensity at 958 cm^{-1} (denoted as I_{958}), and the substitution amount of CO_3^{2-} was examined at its peak intensity at 1074 cm^{-1} (denoted as I_{1074}). The amounts of PO_4^{3-} (I_{958} , Fig. 6b) and CO_3^{2-} (I_{1074} , Fig. 6c) indicated are generally consistent with the distribution of mineralisation in

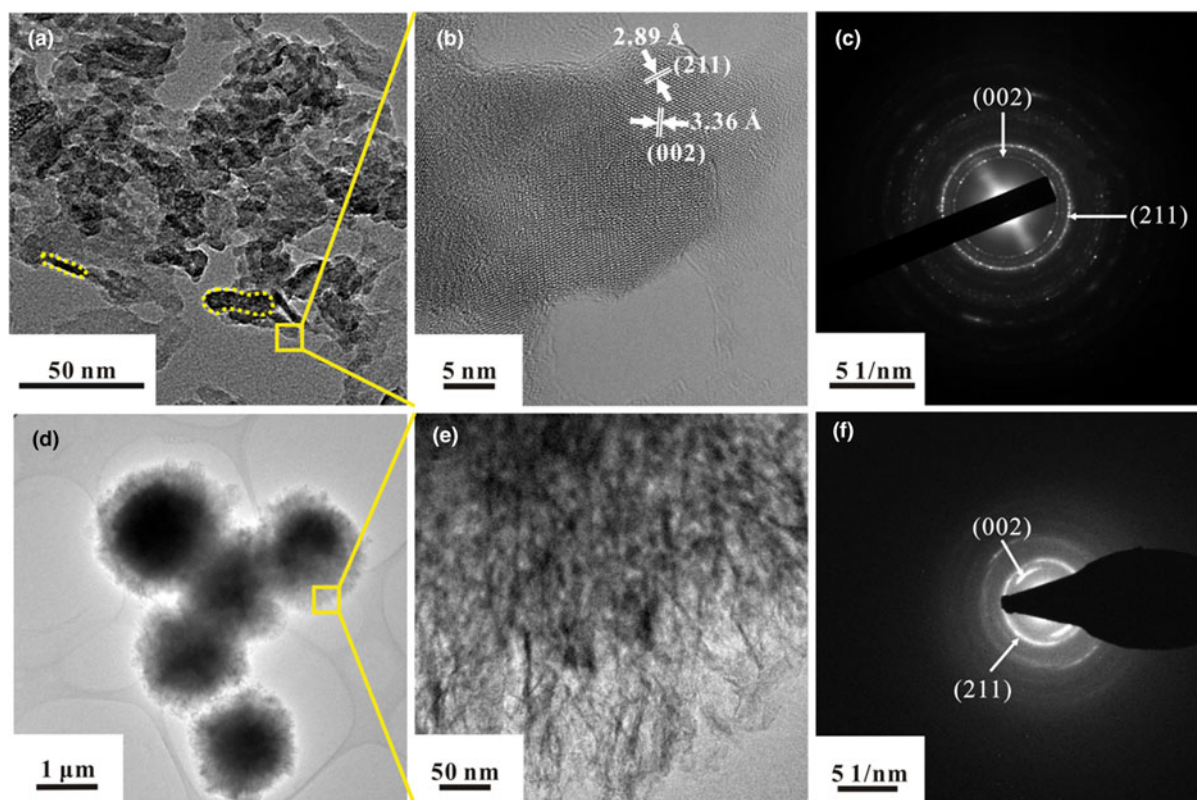


Fig. 4. TEM morphologies (a, d, e), lattice photographs (b), and diffraction patterns (c, f) of calcifications in breast cancer. (a) Short columnar (dotted line, left) or dumbbell-like crystals (dotted line, right) with width of 10–15 nm and length of 20–50 nm. (b) Lattice photograph of the area selected in (a). (c) Diffraction pattern from the area in (b). (d) Spherical calcifications, ~1 μm in diameter. (e) Enlarged view of area selected in (d). (f) Diffraction pattern from the area of (e).

Table 1. EDAX results for breast cancer calcifications.

Element	C	O	Na	Mg	Si	P	S	Ca	Totals
Weight (%)	14.15	41.97	0.42	0.89	5.33	14.07	0.18	22.98	100.00
Atomic (%)	23.2	51.64	0.36	0.72	3.74	8.94	0.11	11.29	

Fig. 6a, and some areas (indicated by the arrow in Fig. 6b) are outside of the mineralised areas visible in the ordinary microscopy image (Fig. 6a), illustrating an inter-relationship between organic tissues and minerals through PO_4^{3-} and CO_3^{2-} . Because the CO_3^{2-} intensity in some areas is low (arrows in Fig. 6c), the I_{958}/I_{1074} ratio was calculated to ascertain the uniformity of $\text{PO}_4^{3-}/\text{CO}_3^{2-}$ in the sample. The results (Fig. 6d) show that the distribution of this ratio is not significantly different from the distribution of calcification itself (Fig. 6a), indicating that the distribution of CO_3^{2-} in mineralisation is broad and uniform.

The strongest peak in the FTIR spectra (Fig. 7) was near 1042 cm^{-1} , and it was assigned as $\nu_3(\text{PO}_4^{3-})$. The $\nu_1(\text{PO}_4^{3-})$ peak at 961 cm^{-1} was very weak, as is common in 'bioapatite', and the $\nu_4(\text{PO}_4^{3-})$ peak at 605 cm^{-1} indicates that the main group of calcifications was PO_4^{3-} (Krajewski *et al.*, 2005; Antonakos *et al.*, 2007). The peaks between 1409 and 1457 cm^{-1} were typical for substitution of PO_4^{3-} by CO_3^{2-} . After fitting, three peaks at approximately 860 , 872 , and 880 cm^{-1} were observed in the 900 – 800 cm^{-1} range. The peaks at 872 and 880 cm^{-1} were assigned to B-type hydroxylapatite (substitution of PO_4^{3-} by CO_3^{2-}) and A-type hydroxylapatite (replacement of OH^- by CO_3^{2-}), respectively. The results

demonstrate that CO_3^{2-} substituted into both PO_4^{3-} and OH^- sites of hydroxylapatite, as in the A–B type substitution (Fleet and Liu, 2003; Antonakos *et al.*, 2007). Ou-Yang *et al.* (2001) reported that the intensity ratio of $\nu_3(\text{CO}_3^{2-})$ to $\nu_3(\text{PO}_4^{3-})$ was linear with percentage of CO_3^{2-} . The percentage ratio of B- to A-type substitution has been estimated based on the intensity ratio of I_{872}/I_{880} (Mangialardo *et al.*, 2012). Table 2 summarises the results of such calculations for 27 cases (the IR spectra of another three cases were of poor quality) examined herein. The CO_3^{2-} content varied from 1.1% to 14.5% with a mean value of 7.3%, which was consistent with typical values for 'bioapatite' (Antonakos *et al.*, 2007; Wang *et al.*, 2018). In all cases, B-type substitution was the dominant type of substitution, and the ratio of B-type to A-type substitution was as high as 18.

Cation substitution

Results from the SR-XRF of the calcifications are compared with a blank 3M film and a hydroxylapatite standard in Fig. 8. Compared to major Ca, the proportions of Zn, Fe and Sr were < 1%. After data fitting for $K\alpha$ peak areas, the presence of trace amounts of Cu, Mn and As were verified. In addition, EDAX also indicated the presence of Na and Mg in the calcifications, although neither Na nor Mg was found in amounts greater than 1 wt.% (Table 1).

The distributions of Ca, P, Mn, Fe, Cu, Zn, As and Sr were examined for a $0.1\text{ mm} \times 0.1\text{ mm}$ area sample of breast cancer tissue (Fig. 9). Calcium and phosphorus, the main elements in hydroxylapatite, were distributed roughly in accordance with the

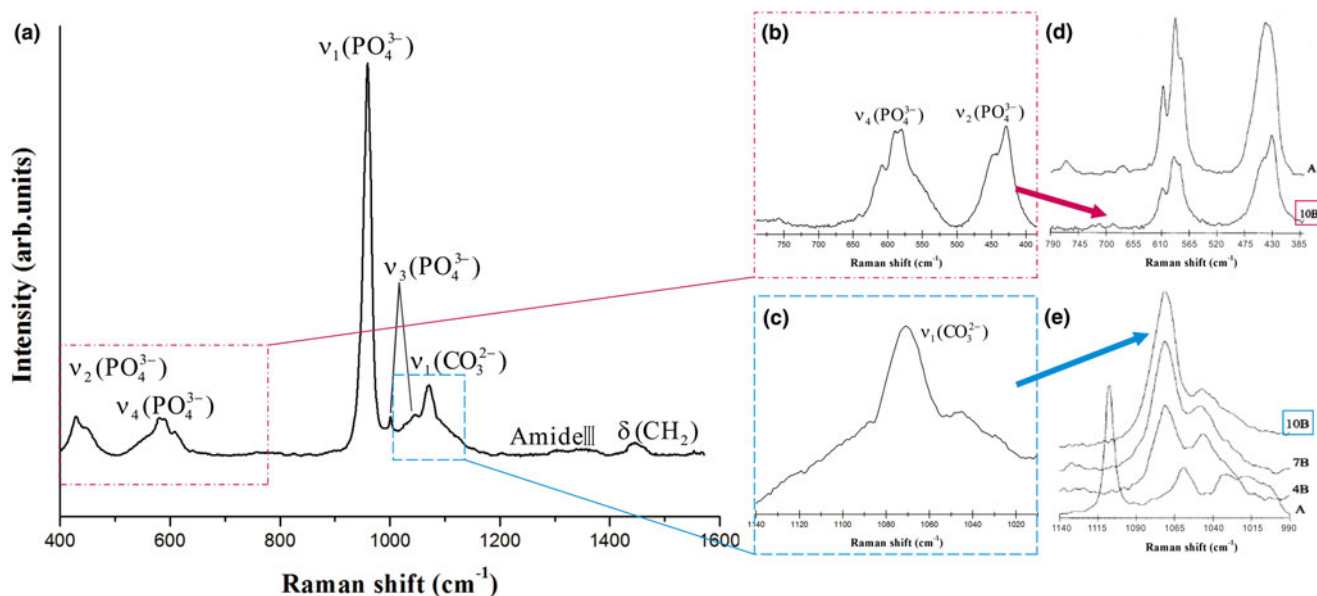


Fig. 5. Raman spectra for breast cancer calcifications. (a) 400–1600 cm^{-1} range. (b) ν_2 and ν_4 modes of PO_4^{3-} (c) ν_1 mode of CO_3^{2-} . (d, e) Reference spectra from Penel *et al.* (1998), where A indicates 5.8 wt.% A-type CO_3^{2-} substitution, and 10B indicates 10 wt.% B-type CO_3^{2-} substitution.

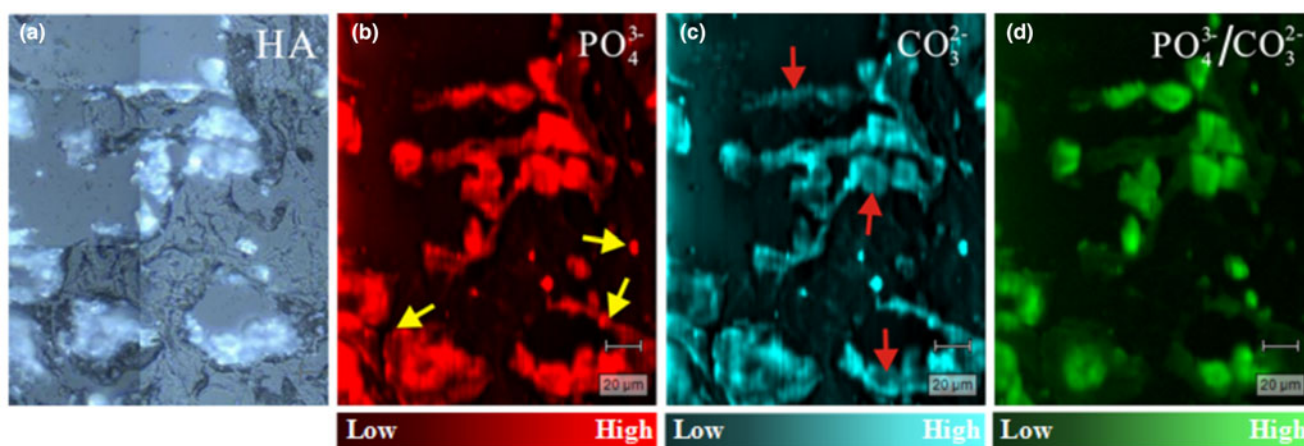


Fig. 6. Raman scattering maps of a breast cancer tissue section. (a) Light-microscope image (50 \times); (b) distribution of PO_4^{3-} (I_{958}); (c) distribution of CO_3^{2-} (I_{1074}); and (d) $\text{PO}_4^{3-}:\text{CO}_3^{2-}$ ratio (I_{958}/I_{1074}). Intensities from low to high are represented by colour brightness; arrowed sites discussed in text.

contours of the calcification. Remarkably, the distribution of Zn showed a higher concentration around the periphery of the calcification than in the centre. Copper, Mn and As were distributed in much smaller amounts within the profile of the calcification, which makes it difficult to compare their distribution patterns with those for Ca and P. Fe was distributed mainly outside the calcification (determined according to the distribution of Ca), and it was associated with the surrounding organs.

Discussion

Carbonate substitution

It is generally accepted that hydroxylapatite is the main mineral phase in breast cancer calcifications (Garola *et al.*, 1978; Panko, 1981; Maaroufi *et al.*, 2000; Tanwell *et al.*, 1994), and the results for all of the cases in this study accord well with previous findings.

The TEM, EDAX, FTIR and Raman results reported herein also indicated the presence of CHA in the calcifications. Carbonated hydroxylapatite 'CHA' has not been designated as a natural mineral by the International Mineralogical Association (IMA) (Pasero *et al.*, 2010), but it has been well-studied in biocalcifications (Penel *et al.*, 1998; Dorozhkin and Epple, 2002; Ivanova *et al.*, 2001), where it is often referred to as 'bioapatite' or biological apatite. The wide range of the Ca:P ratio might be due to interference of organic tissues, involvement of CO_3^{2-} , or calcium deficiency in the crystals.

In all the breast cancer cases we studied, the average CO_3^{2-} level in the calcifications was 7.3%. Previous studies that employed IR spectra to quantify the CO_3^{2-} level of biocalcifications have suggested that the average CO_3^{2-} level in trabecular bone is 6.38% (Ou-yang *et al.*, 2001) and the average CO_3^{2-} level in human heart-valve calcifications is 5–10% (Mangialardo *et al.*, 2012). The CO_3^{2-} content in ash samples from enamel and bone have

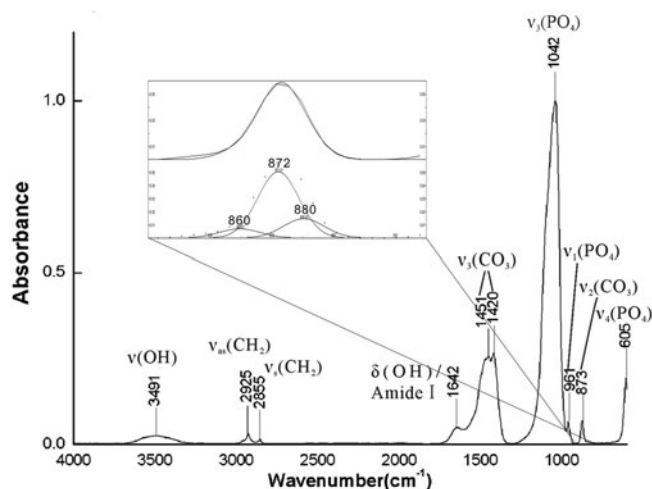


Fig. 7. FTIR spectra of breast cancer calcifications and fitted results in the 900–800 cm^{-1} range.

Table 2. CO_3^{2-} content and ratio of B- to A-type substitution in breast cancer calcifications.

	Min.	Max.	Mean	Average deviation
CO_3^{2-} content (%)	1.1	14.5	7.3	2.5
B-type: A-type substitution	1.1	18.7	7.8	4.7

been estimated to be 4.1 and 6.5 wt.% (Elliott, 2002) and 3.2 and 5.8 wt.% (Gross and Berndt, 2002), respectively. The CO_3^{2-} contents found in enamel, bone, human heart-valve calcifications, and breast cancer calcifications appear to be different. Therefore, the interior environment of the human body may be linked with CO_3^{2-} substitution during intracorporeal calcification.

CO_3^{2-} can substitute into the hydroxylapatite structure at either OH^- or PO_4^{3-} sites, yielding A- or B-type CHA, respectively (LeGeros *et al.*, 1969; Fleet and Liu, 2003; Antonakos *et al.*, 2007). Highly crystalline A-type CHA can be formed by reaction of hydroxylapatite with CO_2 gas at high temperatures (800–1000°C) (Ito *et al.*, 1997), whereas B-type CHA can be formed by precipitation from aqueous media at temperatures of 20–95°C (Krajewski *et al.*, 2005; Merry *et al.*, 1998; Jarcho *et al.*, 1976). Substitution of CO_3^{2-} at the B site has been found to reduce crystallinity and crystal size (Blumenthal and Posner, 1973; Blumenthal *et al.*, 1975; Nelson and Featherstone, 1982), which makes it difficult to characterise it clearly. Because the environment of the human body is comparable to the synthetic conditions that yield B-type CHA, it is not surprising that B-type substitution dominates in breast cancer calcifications. In synthetic experiments, CHA formed at 37°C accommodated the maximum CO_3^{2-} content measured herein (14 wt.%), and B-type substitution was more prevalent (Barralet *et al.*, 1998). However, the pH used (pH >11) during the synthetic experiments is much higher than that found in the fluid environment of the human body (pH \approx 7.5). Therefore, the formation of B-type CHA in breast cancer calcifications may not be the result of an inorganic process but a biological one, and the macromolecules and interstitial fluid around the calcification may account for the regulation of B-type CHA (Blumenthal and Posner, 1973; Rimola *et al.*, 2009; Kato *et al.*, 2015).

Cation substitution and its association with A- or B-type substitution

Regarding cation substitution, we found Na, Mg, Zn, Fe, Sr, Cu, Mn and As in the hydroxylapatite of breast cancer calcifications. Considering that the point of the zero charge (PZC) of hydroxylapatite is fixed at \sim pH 8 (Tarasevich *et al.*, 2012), the surface of hydroxylapatite in standard body fluid (pH 7.3–7.5) thus has a positive charge. Therefore, cations are not likely to be electrostatically adsorbed by hydroxylapatite in this case. According to the foundational theory of isomorphic substitution for the apatite group, the basic requirements for substitution are similar ionic (or atomic) radius, overall charge balance, similar chemical bond and similar thermodynamic conditions (White and Dong, 2003; Pasero *et al.*, 2010). Due to the similar geochemical properties of Ca, Mg and Sr, it is not surprising that Mg and Sr can substitute for Ca in hydroxylapatite, in addition As can replace P (Pasero *et al.*, 2010). In natural geological mineral phases, more than half of the elements that occur as long-lived isotopes can be incorporated into the apatite structure (Hughes and Rakovan, 2015). Therefore, the elements As, Fe, Mg, Mn and Sr often coexist in hydroxylapatite (Pan and Fleet, 2002). Due to the need for similar ionic radius (Table 3) and charge balance for CO_3^{2-} substitution, Na can substitute for Ca (El Feki *et al.*, 2000). Although there are differences between the ionic radius of Zn and Ca, we found that the distribution pattern of Zn was very similar to that of Ca, so there is no doubt that Zn can substitute into the crystal lattice of hydroxylapatite, probably by filling a Ca vacancy, a conclusion that supports the findings of computational modelling (Matsunaga *et al.*, 2010). Other trace elements with smaller ionic radii (Table 3), such as As, Fe, Mn and Cu, can also be adsorbed onto negatively charged sites (Kawasaki *et al.*, 1985). In addition, it is possible for As and, rarely, Mn to enter the crystal structure as AsO_4^{3-} and MnO_4^{3-} substituting for PO_4^{3-} (Pan and Fleet, 2002; Szuszkiewicz *et al.*, 2018). Unfortunately, further confirmation of these mechanisms in breast cancer calcifications was difficult due to their minute amounts, tiny sizes, and the poor crystallinity of hydroxylapatite. Similar mechanisms, however, have been proposed in studies of synthetic hydroxylapatite (Barralet *et al.*, 1998; Gibson and Bonfield, 2002; El Feki *et al.*, 2000; Nelson and Featherstone, 1982; Vignoles *et al.*, 1988; Ivanova *et al.*, 2001).

Carbonate and cation substitutions complicate the structure of hydroxylapatite in breast cancer calcifications and provide multiple routes to charge balance in the crystal lattice. In hydroxylapatite, when CO_3^{2-} replaces OH^- , either more or higher-valence cations are needed for charge balance, unless the ratio of CO_3^{2-} insertion to OH^- removal is 1:2. When CO_3^{2-} substitutes for PO_4^{3-} , fewer cations, lower-valence cations, or Ca vacancies are needed to maintain the charge balance. In breast cancer calcifications, B-type CO_3^{2-} substitution is dominant, so the charge cannot be balanced by the coexistence of B-type and A-type substitutions alone. Therefore, it is not surprising to find Na in the crystal lattice, and Ca vacancies are highly likely.

Diagnostic significance and implications

Isomorphic substitution is very common in ‘bioapatite’ and has been studied extensively in bones and teeth (Johnson *et al.*, 1966; Nemliher *et al.*, 2004; Li and Pasteris, 2014; Seredin *et al.*, 2015), but it has rarely been investigated in breast cancer calcifications (Romaniuk *et al.*, 2016). This work firstly observed that

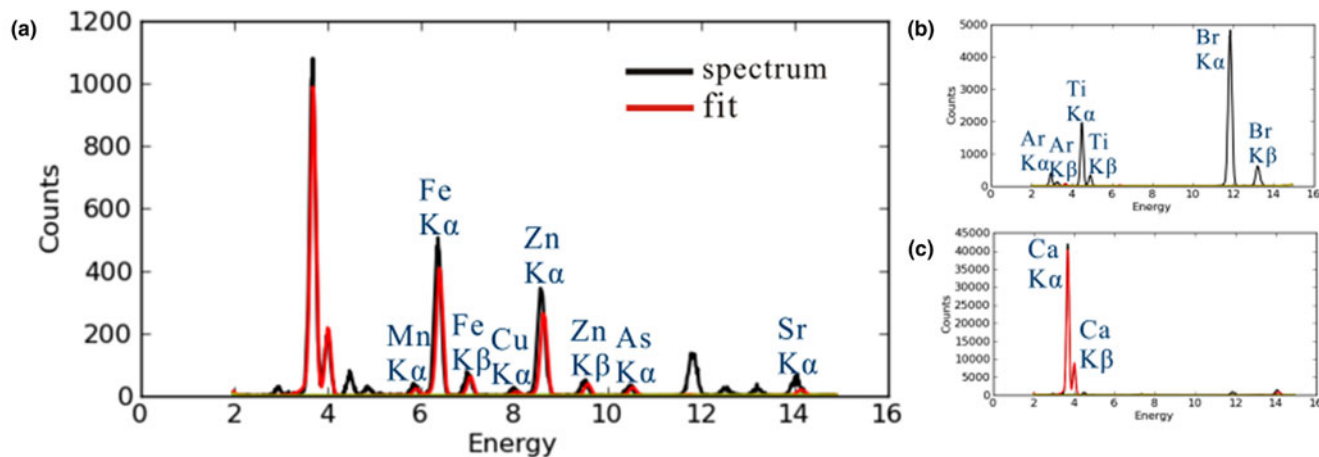


Fig. 8. Fitting curves of SR-XRF results. (a) Breast cancer calcifications; (b) blank 3M film; (c) hydroxylapatite standard. Black line: experimental results; red line: fitting curve.

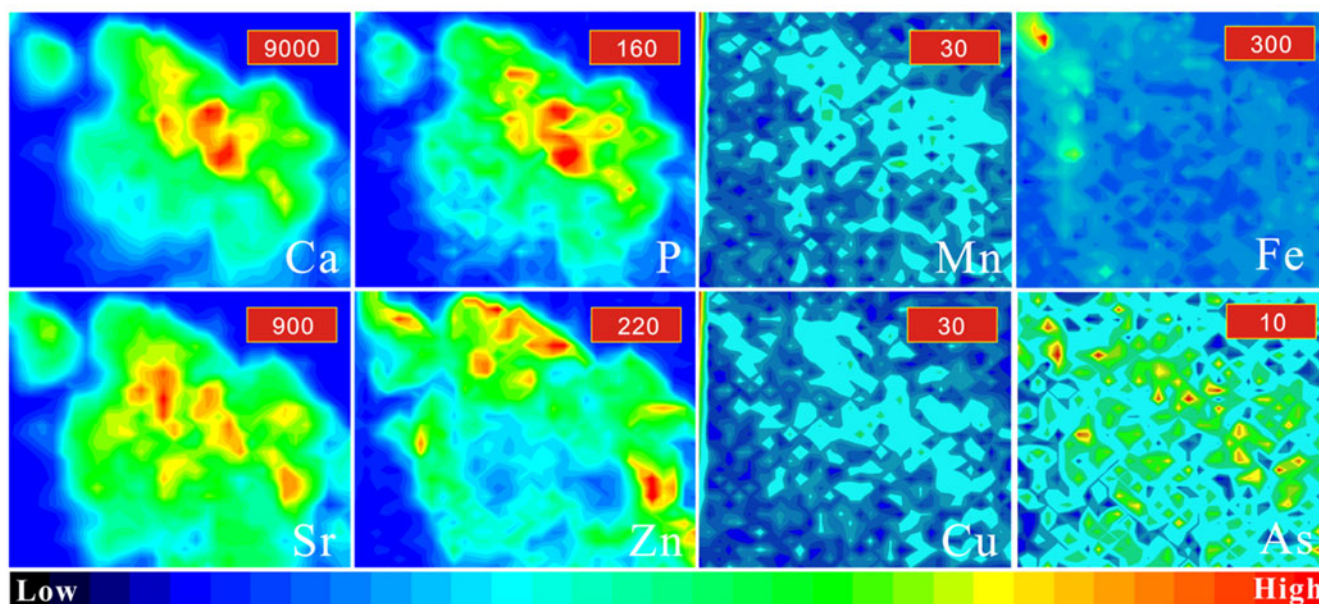


Fig. 9. Distribution of Ca, P, Mn, Zn, Sr, Fe and Cu within a 0.1 mm × 0.1 mm area in breast cancer. Colours from red to blue represent the highest to lowest counts. The maximum counts of each element are listed in the red box in the upper-right corner of each image. The intensities from low to high are represented by different colours.

cations like Na^+ , Mg^{2+} , Zn^{2+} , Fe^{3+} , Sr^{2+} , Cu^{2+} , Mn^{2+} and As^{5+} could coexist in the calcifications, and CO_3^{2-} substitution was dominated by B-type substitution (schematically shown in Fig. 1). Thus, the calcifications seem to be more chemically active than pure hydroxylapatite.

Interactions between organics and calcifications may prove interesting. For example, macromolecules and interstitial fluids adjacent to the calcifications may influence the sites of CO_3^{2-} substitution, as evidenced both by the failure to synthesise B-type CHA under conditions similar to those within the human body (Barralet *et al.*, 1998) and by the large difference between the CO_3^{2-} content found in enamel and breast cancer calcifications. The calculations of CO_3^{2-} content and the ratio of B- to A-type substitution in the calcifications provide quantitative data that

can be used to determine the characteristics of breast cancer from a mineralogical perspective.

The identification of trace elements such as Zn, Fe, Sr, Cu, Mn and As may serve as a useful and promising diagnostic for breast cancer calcifications. Previous studies found that only the elements Ca, P, Mg, S, Na, Cl and K were found in breast cancer calcifications (Ng *et al.*, 1997; Romaniuk *et al.*, 2016; Scimeca *et al.*, 2018), mainly due to the limitations of the measurements. The presence of other trace elements, including the Cu and Zn that we have observed, has great value for breast cancer research. Yücel *et al.* (1994) is the only report of Cu found in patients with breast cancer that were significantly higher than in a control group. Our findings of Cu and Zn in breast cancer calcifications with a uniform distribution show that hydroxylapatite could be

Table 3. Ionic radii of metallic elements found in breast cancer calcifications.

Element	As	Fe	Mn	Mg	Cu	Zn	Ca	Na	Sr
Ionic radius (Å) (valence)	0.34 (+5)	0.645 (+3)	0.67 (+2)	0.72 (+2)	0.73 (+2)	0.74 (+2)	0.99 (+2)	1.02 (+1)	1.12 (+2)

one of the most important sinks of these abnormal elements in the body. In addition, breast cancer tumours were found to have a significantly lighter Zn isotopic composition (-0.6 to -0.9% of $\delta^{66}\text{Zn}$) than healthy breast tissue (-0.3 to -0.5%) as well as blood and serum (-0.1 to $+0.3\%$) in both groups (Larner *et al.*, 2015). Because the trace elements present in breast cancer calcifications are in a relatively stable state, their detection in calcifications will be more meaningful clinically than their detection in the organic tissues. In turn, the development of calcifications can change the local environment as Ca, phosphate ions, and trace elements are accumulated at the calcification site (Cui *et al.*, 2007; Saul, 2009). This process can be considered a type of detoxification (Saul, 2009), because relatively high levels of Zn, Fe and Ca in benign breast tissue may be associated with a modest increase in risk for subsequent breast cancer (Cui *et al.*, 2007).

The concentrations or ratios of trace elements in breast cancer calcifications also have promise for building corresponding diagnostic pools. However, we have not yet found a way to establish a diagnostic pool of this type using current data. Further data is needed and we encourage more mineralogists and materials scientists to join this field to allow sufficient data to be gathered to create a diagnostic pool. The *in situ* micro-mapping of elements based on synchrotron radiation light source as well as micro-Raman and FTIR are an effective method to investigate the distribution and substitution of elements in biogenic microcalcifications.

Conclusions

The breast cancer calcifications investigated were found to consist of either irregular aggregates with widths greater than 200 μm , or spherical aggregates similar to psammoma bodies with an average diameter of 30 μm . Short columnar or dumbbell-shaped aggregates with widths of 10–15 nm and lengths of 20–50 nm were the most common morphologies. Hydroxylapatite was the dominant mineral phase in the calcifications, and both CO_3^{2-} and cation substitutions were present in the hydroxylapatite structure. The appearance in the FTIR spectra of peaks at 872 and 880 cm^{-1} indicated that CO_3^{2-} substituted both PO_4^{3-} and OH^- sites of hydroxylapatite. The ratio of B-type to A-type substitution was estimated to be in the range of 1.1–18.7 from the ratio of the peak intensities (I_{872}/I_{880}), and the CO_3^{2-} contents varied from 1.1% to 14.5%. Trace elements of Na, Mg, Zn, Fe, Sr, Cu, Mn and As were present in the calcifications. Therefore, breast cancer calcifications may provide a diagnostic site for these trace elements.

Acknowledgements. This work was supported by the National Natural Science Foundation of China (4177020314, 41522201) and the DDE-IUGS Big Science Program. We thank the staff at BL15U and SSRF for providing beam time and offering help during the tests.

References

Achal V., Mukherjee A., Kumari D. and Zhang Q. (2015) Biomineralization for sustainable construction – A review of processes and applications. *Earth-Science Reviews*, **148**, 1–17.

- Antonakos A., Liarokapis E. and Leventouri T. (2007) Micro-Raman and FTIR studies of synthetic and natural apatites. *Biomaterials*, **28**, 3043–3054.
- Awonusi A., Morris M.D. and Tecklenburg M.M. (2007) Carbonate assignment and calibration in the Raman spectrum of apatite. *Calcified Tissue International*, **81**, 46–52.
- Baikie T., Ng G.M., Madhavi S., Pramana S.S., Blake K., Elcombe M. and White T.J. (2009) The crystal chemistry of the alkaline-earth apatites $\text{A}_{10}(\text{PO}_4)_6\text{Cu}_x\text{O}_y(\text{H})_z$ (A = Ca, Sr and Ba). *Dalton Transactions*, **34**, 6722–6726.
- Baker R., Rogers K. D., Shepherd N. and Stone N. (2010) New relationships between breast microcalcifications and cancer. *British Journal of Cancer*, **103**, 1034–1039.
- Baldassarre F., Altomare A., Corriero N., Mesto E., Lacalamera M., Bruno G., Sacchetti A., Dida B., Karaj D., Ventura G.D. *et al.* (2020) Crystal chemistry and luminescence properties of Eu-doped polycrystalline hydroxyapatite synthesized by chemical precipitation at room temperature. *Crystals*, **10**, 250.
- Barralet J., Best S. and Bonfield W. (1998) Carbonate substitution in precipitated hydroxyapatite: an investigation into the effects of reaction temperature and bicarbonate ion concentration. *Journal of Biomedical Materials Research*, **41**, 79–86.
- Belousova E.A., Griffin W.L., O'Reilly S.Y. and Fisher N.I. (2002) Apatite as an indicator mineral for mineral exploration: trace-element compositions and their relationship to host rock type. *Journal of Geochemical Exploration*, **76**, 45–69.
- Blumenthal N.C. and Posner A.S. (1973) Hydroxyapatite: mechanism of formation and properties. *Calcified Tissue Research*, **13**, 235–243.
- Blumenthal N.C., Betts F. and Posner A.S. (1975) Effect of carbonate and biological macromolecules on formation and properties of hydroxyapatite. *Calcified Tissue Research*, **18**, 81–90.
- Bray F., Ferlay J., Soerjomataram I., Siegel R.L., Torre L.A. and Jemal A. (2018) Global cancer statistics 2018: GLOBOCAN estimates of incidence and mortality worldwide for 36 cancers in 185 countries. *CA: A Cancer Journal for Clinicians*, **68**, 394–424.
- Cheng G., Zhang Y., Yin H., Ruan Y., Sun Y. and Lin K. (2019) Effects of strontium substitution on the structural distortion of hydroxyapatite by Rietveld refinement and Raman Spectroscopy. *Ceramics International*, **45**, 11073–11078.
- Cooke M.M., McCarthy G.M., Sallis J.D. and Morgan M.P. (2003) Phosphocitrate inhibits calcium hydroxyapatite induced mitogenesis and upregulation of matrix metalloproteinase-1, interleukin-1 β and cyclooxygenase-2 mRNA in human breast cancer cell lines. *Breast Cancer Research and Treatment*, **79**, 253–263.
- Cui Y., Vogt S., Olson N., Glass A.G. and Rohan T.E. (2007) Levels of zinc, selenium, calcium, and iron in benign breast tissue and risk of subsequent breast cancer. *Cancer Epidemiology and Prevention Biomarkers*, **16**, 1682–1685.
- Dorozhkin S.V. and Epple M. (2002) Biological and medical significance of calcium phosphates. *Angewandte Chemie International Edition*, **41**, 3130–3146.
- El Feki H., Savariault J.M. and Salah A.B. (1999) Structure refinements by the Rietveld method of partially substituted hydroxyapatite: $\text{Ca}_9\text{Na}_{0.5}(\text{PO}_4)_{4.5}(\text{CO}_3)_{1.5}(\text{OH})_2$. *Journal of Alloys and Compounds*, **287**, 114–120.
- El Feki H., Savariault J.M., Salah A.B. and Jemal M. (2000) Sodium and carbonate distribution in substituted calcium hydroxyapatite. *Solid State Sciences*, **2**, 577–586.
- Elliott J.C. (2002) Calcium phosphate biominerals. Pp. 427–453 in: *Phosphates* (M.L. Kohn, J. Rakovan and J.M. Hughes, editors) Reviews in Mineralogy and Geochemistry, **48**. Mineralogical Society of America and the Geochemical Society, Washington DC.
- Fleet M.E. (2009) Infrared spectra of carbonate apatites: ν_2 -Region bands. *Biomaterials*, **30**, 1473–1481.

- Fleet M.E. and Liu X. (2003) Carbonate apatite type A synthesized at high pressure: new space group (P3) and orientation of channel carbonate ion. *Journal of Solid State Chemistry*, **174**, 412–417.
- Fleet M.E., Liu X. and Liu X. (2011) Orientation of channel carbonate ions in apatite: Effect of pressure and composition. *American Mineralogist*, **96**, 1148–1157.
- Frappart L., Remy I., Lin H.C., Bremond A., Raudrant D., Grousson B. and Vauzelle J.L. (1987) Different types of microcalcifications observed in breast pathology. *Virchows Archiv A*, **410**, 179–187.
- Garola R.E. and McGuire W.L. (1978) A hydroxylapatite micromethod for measuring estrogen receptor in human breast cancer. *Cancer Research*, **38**, 2216–2220.
- Get'man E.I., Loboda S.N., Tkachenko T.V., Yablochkova N.V. and Chebyshev K.A. (2010) Isomorphous substitution of samarium and gadolinium for calcium in hydroxyapatite structure. *Russian Journal of Inorganic Chemistry*, **55**, 333–338.
- Gibson I.R. and Bonfield W. (2002) Novel synthesis and characterization of an AB-type carbonate-substituted hydroxyapatite. *Journal of Biomedical Materials Research*, **59**, 697–708.
- Gosling S., Scott R., Greenwood C., Bouzy P., Nallala J., Lyburn I.D., Stone N. and Rogers K. (2019) Calcification microstructure reflects breast tissue microenvironment. *Journal of Mammary Gland Biology and Neoplasia*, **24**, 333–342.
- Gross K.A. and Berndt C.C. (2002) Biomedical application of apatites. Pp. 631–672 in: *Phosphates* (M.L. Kohn, J. Rakovan and J.M. Hughes, editors). Reviews in Mineralogy and Geochemistry, **48**. Mineralogical Society of America and the Geochemical Society, Washington DC.
- Gülsün M., Demirkazık F.B. and Arıyürek M. (2003) Evaluation of breast microcalcifications according to Breast Imaging Reporting and Data System criteria and Le Gal's classification. *European Journal of Radiology*, **47**, 227–231.
- Haka A.S., Shafer-Peltier K.E., Fitzmaurice M., Crowe J., Dasari R.R. and Feld M.S. (2002) Identifying microcalcifications in benign and malignant breast lesions by probing differences in their chemical composition using Raman spectroscopy. *Cancer Research*, **62**, 5375–5380.
- Hammerley A.P. (1997) *FIT2D: An introduction and overview*. ESRF Internal Rep. ESRF97HA02T, European Synchrotron Radiation Facility, Grenoble, France.
- Hughes J.M. and Rakovan J.F. (2015) Structurally robust, chemically diverse: apatite and apatite supergroup minerals. *Elements*, **11**, 165–170.
- Ito A., Maekawa K., Tsutsumi S., Ikazaki F. and Tateishi T. (1997) Solubility product of OH-carbonated hydroxyapatite. *Journal of Biomedical Materials Research*, **36**, 522–528.
- Ivanova T.I., Frank-Kamenetskaya O.V., Kol'tsov A.B. and Ugolkov V.L. (2001) Crystal structure of calcium-deficient carbonated hydroxyapatite. Thermal decomposition. *Journal of Solid State Chemistry*, **160**, 340–349.
- Jarcho M., Bolen C.H., Thomas M.B., Bobick J., Kay J.F. and Doremus R.H. (1976) Hydroxylapatite synthesis and characterization in dense polycrystalline form. *Journal of Materials Science*, **11**, 2027–2035.
- Johnson A.R., Armstrong W.D. and Singer L. (1966) Strontium incorporation into dental enamel. *Science*, **153**, 1396–1397.
- Kaltenbach B., Brandebusch V., Möbus V., Mall G., Falk S., van den Bergh M., Chevalier F. and Müller-Schimpfle M. (2017) A matrix of morphology and distribution of calcifications in the breast: analysis of 849 vacuum-assisted biopsies. *European Journal of Radiology*, **86**, 221–226.
- Kato K., Fukuzawa K. and Mochizuki Y. (2015) Modeling of hydroxyapatite-peptide interaction based on fragment molecular orbital method. *Chemical Physics Letters*, **629**, 58–64.
- Kawasaki T., Takahashi S. and Iweda K. (1985) Hydroxyapatite high-performance liquid chromatography: column performance for proteins. *European Journal of Biochemistry*, **152**, 361–371.
- Krajewski A., Mazzocchi M., Buldini P.L., Ravaglioli A., Tinti A., Taddei P. and Fagnano C. (2005) Synthesis of carbonated hydroxyapatites: efficiency of the substitution and critical evaluation of analytical methods. *Journal of Molecular Structure*, **744**, 221–228.
- Kunitake J.A., Choi S., Nguyen K.X., Lee M.M., He F., Sudilovsky D., Morris P.G., Jochelson M.S., Hudis C.A., Muller D.A. et al. (2018) Correlative imaging reveals physicochemical heterogeneity of microcalcifications in human breast carcinomas. *Journal of Structural Biology*, **202**, 25–34.
- Lala S., Ghosh M., Das P.K., Das D., Kar T. and Pradhan S.K. (2016) Magnesium substitution in carbonated hydroxyapatite: structural and microstructural characterization by Rietveld's refinement. *Materials Chemistry and Physics*, **170**, 319–329.
- Larner F., Woodley L.N., Shousha S., Moyes A., Humphreys-Williams E., Strekopytov S., Halliday A.N., Rehkämper M. and Coombes R.C. (2015) Zinc isotopic compositions of breast cancer tissue. *Metallomics*, **7**, 112–117.
- Legeros R.Z., Trautz O.R., Legeros J.P., Klein E. and Shirra W.P. (1967) Apatite crystallites: effects of carbonate on morphology. *Science*, **155**, 1409–1411.
- LeGeros R.Z., Trautz O.R., Klein E. and LeGeros J.P. (1969) Two types of carbonate substitution in the apatite structure. *Experientia*, **25**, 5–7.
- LeGeros R.Z., Miravite M.A., Quiroigco G.B. and Curzon M.E.J. (1976) The effect of some trace elements on the lattice parameters of human and synthetic apatites. *Calcified Tissue Research*, **22**, 362–367.
- Li Z. and Pasteris J.D. (2014) Chemistry of bone mineral, based on the hypermineralized rostrum of the beaked whale *Mesoplodon densirostris*. *American Mineralogist*, **99**, 645–653.
- Li Z.Y., Lam W.M., Yang C., Xu B., Ni G.X., Abbah S.A., Cheung K.M.C., Luk K.D.K. and Lu W.W. (2007) Chemical composition, crystal size and lattice structural changes after incorporation of strontium into biomimetic apatite. *Biomaterials*, **28**, 1452–1460.
- Lieberman L., Abramson A.F., Squires F.B., Glassman J.R., Morris E.A. and Dershaw D.D. (1998) The breast imaging reporting and data system: positive predictive value of mammographic features and final assessment categories. *AJR. American Journal of Roentgenology*, **171**, 35–40.
- Maaroufi Y., Lacroix M., Lespagnard L., Journé F., Larsimont D. and Leclercq G. (2000) Estrogen receptor of primary breast cancers: evidence for intracellular proteolysis. *Breast Cancer Research*, **2**, 1–11.
- Madupalli H., Pavan B. and Tecklenburg M.M. (2017) Carbonate substitution in the mineral component of bone: Discriminating the structural changes, simultaneously imposed by carbonate in A and B sites of apatite. *Journal of Solid State Chemistry*, **255**, 27–35.
- Mangialardo S., Cottignoli V., Cavarretta E., Salvador L., Postorino P. and Maras A. (2012) Pathological biominerals: Raman and infrared studies of bioapatite deposits in human heart valves. *Applied Spectroscopy*, **66**, 1121–1127.
- Matsunaga K., Murata H., Mizoguchi T. and Nakahira A. (2010) Mechanism of incorporation of zinc into hydroxyapatite. *Acta Biomaterialia*, **6**, 2289–2293.
- McConnell D. (1960) The stoichiometry of hydroxyapatite. *Naturwissenschaften*, **47**, 227–227.
- Merry J.C., Gibson I.R., Best S.M. and Bonfield W. (1998) Synthesis and characterization of carbonate hydroxyapatite. *Journal of Materials Science*, **9**, 779–783.
- Mills S.J. and Christy A.G. (2016) The Great Barrier Reef Expedition 1928–29: The crystal structure and occurrence of weddellite, ideally $\text{CaC}_2\text{O}_4 \cdot 2.5\text{H}_2\text{O}$, from the Low Isles, Queensland. *Mineralogical Magazine*, **80**, 399–406.
- Morgan M.P., Cooke M.M., Christopherson P.A., Westfall P.R. and McCarthy G.M. (2001) Calcium hydroxyapatite promotes mitogenesis and matrix metalloproteinase expression in human breast cancer cell lines. *Molecular Carcinogenesis*, **32**, 111–117.
- Nelson D.G. and Featherstone J.D. (1982) Preparation, analysis, and characterization of carbonated apatites. *Calcified Tissue International*, **34**, S69–81.
- Nemliher J.G., Baturin G.N., Kallaste T.E. and Murdmaa I.O. (2004) Transformation of hydroxyapatite of bone phosphate from the ocean bottom during fossilization. *Lithology and Mineral Resources*, **39**, 468–479.
- Ng K., Looi L. and Bradley D. (1997) The elemental composition of breast tissue: Can this be related to breast particle deposition? *Journal of Radioanalytical and Nuclear Chemistry*, **217**, 193–199.
- Obadia L., Amador G., Daculsi G. and Bouler J.M. (2003) Calcium-deficient apatite: influence of granule size and consolidation mode on release and in vitro activity of vancomycin. *Biomaterials*, **24**, 1265–1270.
- Obenauer S., Hermann K.P. and Grabbe E. (2005) Applications and literature review of the BI-RADS classification. *European Radiology*, **15**, 1027–1036.
- Ou-Yang H., Paschalis E.P., Mayo W.E., Boskey A.L. and Mendelsohn R. (2001) Infrared microscopic imaging of bone: spatial distribution of CO_3^{2-} . *Journal of Bone and Mineral Research*, **16**, 893–900.
- Pan Y. and Fleet M.E. (2002) Compositions of the apatite-group minerals: substitution mechanisms and controlling factors. Pp. 13–49 in: *Phosphates* (M.L. Kohn, J. Rakovan and J.M. Hughes, editors). Reviews in

- Mineralogy and Geochemistry, **48**. Mineralogical Society of America and the Geochemical Society, Washington DC.
- Panko W.B., Watson C.S. and Clark J.H. (1981) The presence of a second, specific estrogen binding site in human breast cancer. *Journal of Steroid Biochemistry*, **14**, 1311–1316.
- Pasero M., Kampf A.R., Ferraris C., Pekov I.V., Rakovan J. and White T.J. (2010) Nomenclature of the apatite supergroup minerals. *European Journal of Mineralogy*, **22**, 163–179.
- Penel G., Leroy G., Rey C. and Bres E. (1998) MicroRaman spectral study of the PO₄ and CO₃ vibrational modes in synthetic and biological apatites. *Calcified Tissue International*, **63**, 475–481.
- Peroos S., Du Z. and de Leeuw N.H. (2006) A computer modelling study of the uptake, structure and distribution of carbonate defects in hydroxy-apatite. *Biomaterials*, **27**, 2150–2161.
- Raynaud S., Champion E., Bernache-Assollant D. and Thomas P. (2002) Calcium phosphate apatites with variable Ca/P atomic ratio I. Synthesis, characterisation and thermal stability of powders. *Biomaterials*, **23**, 1065–1072.
- Rimola A., Corno M., Zicovich-Wilson C.M. and Ugliengo P. (2009) *Ab initio* modeling of protein/biomaterial interactions: competitive adsorption between glycine and water onto hydroxyapatite surfaces. *Physical Chemistry Chemical Physics*, **11**, 9005–9007.
- Romaniuk A.M., Lyndin M.S., Moskalenko R.A., Hortynska O.M. and Lyndina Y.M. (2016) The role of heavy metal salts in pathological biomineralization of breast cancer tissue. *Advances in Clinical and Experimental Medicine*, **25**, 907–910.
- Sathyavathi R., Saha A., Soares J.S., Spegazzini N., McGee S., Dasari R.R., Fitzmaurice M and Barman I. (2015) Raman spectroscopic sensing of carbonate intercalation in breast microcalcifications at stereotactic biopsy. *Scientific Reports*, **5**, 1–12.
- Saul J.M. (2009) Did detoxification processes cause complex life to emerge? *Lethaia*, **42**, 179–184.
- Scimeca M., Bischetti S., Lamsira H.K., Bonfiglio R. and Bonanno E. (2018) Energy Dispersive X-ray (EDX) microanalysis: A powerful tool in biomedical research and diagnosis. *European Journal of Histochemistry: EJH*, **62**, 2841
- Seredin P., Goloshchapov D., Prutskij T. and Ippolitov Y. (2015) Phase transformations in a human tooth tissue at the initial stage of caries. *PLoS One*, **10**, e0124008.
- Shen Y., Liu J., Lin K. and Zhang W. (2012) Synthesis of strontium substituted hydroxyapatite whiskers used as bioactive and mechanical reinforcement material. *Materials Letters*, **70**, 76–79.
- Solé V.A., Papillon E., Cotte M., Walter P. and Susini J.A. (2007) A multiplatform code for the analysis of energy-dispersive X-ray fluorescence spectra. *Spectrochimica Acta*, **B62**, 63–68.
- Szuskiewicz A., Pieczka A., Gołębiewska B., Dumańska-Słowik M., Marszałek M. and Szełęg E. (2018) Chemical composition of Mn- and Cl-rich apatites from the Szklary pegmatite, Central Sudetes, SW Poland: Taxonomic and genetic implications. *Minerals*, **8**, 350.
- Tanwell C.S., Gescher A., Bradshaw T.D. and Pettit G.R. (1994) The role of protein kinase C isoenzymes in the growth inhibition caused by bryostatins 1 in human A549 lung and MCF-7 breast carcinoma cells. *International Journal of Cancer*, **56**, 585–592.
- Tarasevich Y.I., Shkutkova E.V. and Janusz W. (2012) Sorption of ions of heavy metals from aqueous solutions on hydroxylapatite. *Journal of Water Chemistry and Technology*, **34**, 125–132.
- Vignoles M., Bonel G., Holcomb D.W. and Young R.A. (1988) Influence of preparation conditions on the composition of type B carbonated hydroxyapatite and on the localization of the carbonate ions. *Calcified Tissue International*, **43**, 33–40.
- Wang C., Yang R., Li Y., Xiong C., Zhao W., Liu J., Zhang B. and Lu A. (2011) A study on psammoma body mineralization in meningiomas. *Journal of Mineralogical and Petrological Sciences*, **106**, 229–234.
- Wang M., Qian R., Bao M., Gu C. and Zhu P. (2018) Raman, FTIR and XRD study of bovine bone mineral and carbonated apatites with different carbonate levels. *Materials Letters*, **210**, 203–206.
- Webster T.J., Ergun C., Doremus R.H. and Bizios R. (2002) Hydroxylapatite with substituted magnesium, zinc, cadmium, and yttrium. II. Mechanisms of osteoblast adhesion. *Journal of Biomedical Materials Research*, **59**, 312–317.
- Weiner S. and Dove P.M. (2003) An overview of biomineralization processes and the problem of the vital effect. Pp. 1–29 in: *Biomineralisation* (P.M. Dove, S. Weiner and J.J. De Yoreo, editors). Reviews in Mineralogy and Geochemistry, **54**. Mineralogical Society of America and the Geochemical Society, Washington DC.
- White T.J. and Dong Z. (2003) Structural derivation and crystal chemistry of apatites. *Acta Crystallographica*, **B59**, 1–16.
- World Health Organization (2017) Guide to cancer early diagnosis. World Health Organization. <https://apps.who.int/iris/handle/10665/254500>.
- Yücel I., Arpacı F., Özet A., Döner B., Karayılanoğlu T., Sayar A. and Berk Ö. (1994) Serum copper and zinc levels and copper/zinc ratio in patients with breast cancer. *Biological Trace Element Research*, **40**, 31–38.